Colloids and Surfaces A: Physicochem. Eng. Aspects 498 (2016) 168–175

Contents lists available at ScienceDirect

Colloids and Surfaces A: Physicochemical and Engineering Aspects

journal homepage: www.elsevier.com/locate/colsurfa

Engineering microscale two-dimensional gold nanoparticle cluster arrays for advanced Raman sensing: An AFM study

F. Domenici[a,b,*], C. Fasolato[a,c], E. Mazzi[a,d], L. De Angelis[a,e], F. Brasili[a], F. Mura[f], P. Postorino[a], F. Bordi[a,g]

[a] Dipartimento di Fisica, Sapienza Università di Roma, P.le A. Moro 5, 00185 Roma, Italy
[b] Dipartimento di Scienze e Tecnologie Chimiche, Università di Roma Tor Vergata, Via Della Ricerca Scientifica, 00133 Roma, Italy
[c] Center for Life Nanoscience@Sapienza, Istituto Italiano di Tecnologia, V.le Regina Elena, 291, 00185 Roma, Italy
[d] Physics of Complex Fluids Group, MESA+ Institute, University of Twente, P.O. Box 217, 7500 AE Enschede, The Netherlands
[e] Center for Nanophotonics, FOM Institute AMOLF, Science Park 104, 1098 XG Amsterdam, The Netherlands
[f] Dipartimento di Chimica, Sapienza Università di Roma, P.le A. Moro 5, 00185 Roma, Italy
[g] CNR-ISC UOS Roma, Sapienza Università di Roma, P.le A. Moro 5, 00185 Roma, Italy

HIGHLIGHTS

- Design and AFM analysis of nanoparticle cluster arrays for improved Raman sensing.
- Electron beam lithography templates were optimized by varying the e-beam dose.
- Tightly packed and regularly shaped 2D gold nanoparticle assemblies were reached.
- The microsized clusters provided a huge and reproducible gain of the Raman signal.

GRAPHICAL ABSTRACT

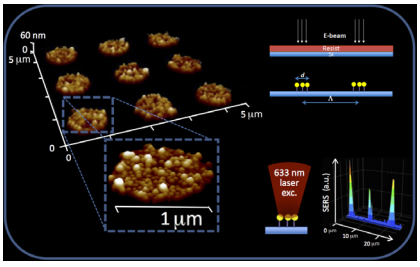

ARTICLE INFO

Article history:
Received 10 December 2015
Received in revised form 13 March 2016
Accepted 14 March 2016
Available online 16 March 2016

Keywords:
AFM
Nanoparticle clusters
Array
EBL
Surface-enhanced raman scattering

ABSTRACT

We realized and tested a strategy for developing reproducible and stable two-dimensional gold nanoparticle cluster arrays arranged on silicon substrates, to be used for surface-enhanced Raman spectroscopy. We combined electron beam lithography and molecular functionalization to finely control the shape of the nanoparticle assemblies. Atomic force microscopy analysis allowed to optimize the procedure of nanoparticle cluster array fabrication in terms of electron beam dose and chemical protocol, enabling to achieve a good regularity in spacing and size (i.e. area and layer number) of the clusters. MicroRaman space resolved measurements were undertaken on large 2D arrays ($100 \times 100\ \mu m^2$) made up of regularly microsized clusters. The high surface enhanced Raman signal measured on the structures highlights the full correspondence of the spatial and optical periodicity achieved. This standardized procedure represent the basis to realize versatile platforms for nano-optical investigation and towards an efficient high-sensitive multiplex sensing.

1. Introduction

An important challenge for nanosensing investigation is the design of improved tools to overcome uncertainties and shortcomings of current diagnostics [1–5]. This goal can be concretized

* Corresponding author.
E-mail addresses: fabiodomenici@gmail.com (F. Domenici), paolo.postorino@roma1.infn.it (P. Postorino), federico.bordi@roma1.infn.it (F. Bordi).

http://dx.doi.org/10.1016/j.colsurfa.2016.03.043
0927-7757/

realizing ultrasensitive and molecular specific detection substrates using gold nanoparticles (NPs) [2–6]. The rationale of the gold NPs choice lies in their peculiar properties of a high surface-to-volume ratio, the possibility of suitable biomolecular conjugation [7–9], their rewarding chemical stability [7–9], and the collective electronic behavior at their surface [10,11]. In particular, their electromagnetic signal enhancement capability [10–12], combined with their ability to form hybrid assemblies with biomolecules [3,4,8], provides the basis to probe molecular structures and conformation of biomolecules at extraordinarily low concentration with spectroscopic tools. In this frame, we previously enlightened [13] the role of spontaneous mesoscopic architectures, (NP clusters self-assembled on solid supports), in providing a huge and size dependent enhancement of the Raman signal of the analyte confined within. Analogously to single plasmonic objects, close packed NP aggregates can induce the confinement of intense electromagnetic fields at their surface [13]. The Raman scattered intensity increases linearly with the NP cluster area (up to $\sim$30 μm^2), exhibiting different slopes depending on the aggregate thickness. Such dependence on the thickness, allows to ascribe the increased variability of the Raman intensity observed in larger clusters to their intrinsically higher inhomogeneity (variability of layer number) [13,14]. These findings suggest that ordered, closely packed single layered "patches" of NP measuring a few squared microns could guarantee an easy recognition of these aggregates within the optical resolution of a microoptical apparatus, a good enhancement of the Raman signal, and a reduced Raman intensity variability [3,15,16]. However, although micrometric fractal assemblies are easy and economical to generate, the reproducibility of the giant Raman scattering enhancements are difficult to control in such completely random structures.

Colloidal NPs can be assembled into deterministic arrays using top-down lithographic methods with excellent reproducibility, such as focused ion beam techniques or Electron Beam Lithography (EBL) [17,18]. The latter has recently emerged as a flexible and quick tool for extensive nano- and micro-patterning, avoiding effects of ion implantation in exposed sites [17]. Unfortunately to date, it remains tricky to generate NP sites with gaps of less than a few tenths-nm, with the disadvantage that the Raman intensities arising from the so obtained architectures is significantly smaller than those achieved in "chemically" assembled clusters of nearly touching NPs [6]. Consequently, rational nanofabrication methods have to be tailored to create some challenging molecular and microorganisms sensing platforms made up of strongly coupled NP clusters of well defined microscale area and morphology [16].

Proceeding from this, we combined EBL and self-assembly strategies [19–21] to develop novel two-dimensional arrays of mesoscopic NPs aggregates with well-defined shape yielding a well-predictable Raman field enhancement. Template guided self-assembly can in facts induce gold NP aggregation in different, regular Nanoparticle Cluster Arrays (NCA) platforms, very promising for applications, where the reproducibility of the clustered NP patches in terms of shape, size and thickness are crucial for their optical response. In addition, the flexibility of the NCA fabrication approach makes it straightforward to adjust the electromagnetic response of NCAs, varying the value of the characteristic parameters [3,15,16,22].

Within these purposes, the first step in NCA fabrication is optimizing the electron beam (e-beam) dose value with respect to the reproducibility of the mask geometry involved. There is a trade-off among speed, complexity and accuracy in the EBL writing of a desired mask. High energy e-beam is used for optimal resolution, although electron scattering limits its application, particularly due to the "proximity effect", where electrons writing a feature at one location overexpose a nearby feature, affecting the pattern geometry [23,24]. The second necessary step is to frame the chemical derivatization strategy of the EBL patterned surface in order to assure a selective and tight covering of the NPs (60 nm sized) on the printed pattern.

The mesoscopic size of the cluster composing our NCA allows an easily determination of their position by optical imaging. However, in order to gain detailed information on the shape of the patches and their ordering and thickness we performed an accurate Atomic Force Microscopy (AFM) analysis. The optical, microRaman and AFM combined imaging on the NCA functionalized with a Raman marker show an excellent correspondence between the optical and the topographic array maps. The high enhancement factor and the quite good reproducibility of the Raman sensing are promising for the implementation of multiplexed sensing on this kind of substrates. Indeed, the regular, geometrical 2D disposition of the clusters on the substrate allows to perform multiple measurements on a single sample, with the possibility of a careful statistical analysis of the collected data. Moreover, the nature of the substrate paves the way for the implementation of multiplexed sensing platform.

2. Experimental

2.1. Electron beam lithography setup

EBL was performed using a Zeiss Auriga 405 Field Emission Microscope equipped with a Raith Elphy Quantum EBL module (c/o SNN-Lab—Sapienza Nanoscience & Nanotechnology Lab). Before starting the lithographic process, (100)-oriented silicon wafers were cleaned in absolute ethanol (organic cleaning) and then sonicated (mechanical cleaning) for 2 min. Afterwards the wafer was placed in boiling 1,1,1-trichloroethane for 10 min and rinsed with milli-Q water. The treatment with an oxidizing solution increases the number of the exposed Si—OH bonds, involved in the linkage with NPs, on the wafer surface. The positive resist AR P632.04 (purchased from ALLRESIST GmbH, Germany) was employed to obtain a silicon-supported poly-methylmethacrylate (PMMA) film through the spin-coating technique. After several preliminary tests we established a working protocol, with a spin rate of 3000 r.p.m., that ensures the deposition of a thin and uniform solid PMMA layer. After the resist coating, the sample was baked in the oven at 120 °C for 1 h. This thermal annealing procedure stabilizes the film structure cross-linking the chemical groups, removes the residual solvent, and the stress built up in the resist during the spinning session [25]. The Atomic Force Microscopy (AFM) profilometry evaluated an almost constant resist thickness of $\sim$60 nm (see also Section 3.1). This steady thickness guarantees an accurate lithography with a regular and well-defined micro-patterning of the substrate. Being the thickness of the written PMMA comparable or smaller (Fig. S1a–c) than the NPs diameter, once the substrate has been developed the surface functionalized and the particles deposited, the particles protrude partially out of the well above the PMMA surface. In this way, measuring the AFM profiles, we were able to investigate in details, the effective immobilization and the packing of the NPs on the masked resist surface, and therefore the reproducibility of the whole substrate fabrication procedure.

The layout of the desired pattern was designed using the Computer-Aided Design (CAD) program of the EBL module. On each sample, several pattern configurations (or sectors) were realized, varying the diameter of the binding sites, d, and their periodical separation, Λ. The working parameters used were step size and line spacing of 24 nm, dwell time of 6×10^{-4} ms and two different area dose values (100 $\mu C/cm^2$ and 20 $\mu C/cm^2$). The dose is defined as the product of beam current and beam dwell time, that is the time taken for the electrons to penetrate the resist.

The e-beam exposed substrates were then treated with the developer AR 600–55 (ALLRESIST GmbH, Germany) for 60 s, to

favour a high solubility of the resist areas impinged by the e-beam. The substrates were then transferred into the stopper bath AR 600–60 (ALLRESIST GmbH, Germany) for 30 s. This solution interrupted the development process and lead to a rapid rinsing of the residual developer. Then, the substrates were rinsed in Milli-Q water and dried. After the development, the substrates were baked again for 30 min to thermally anneal the exposed regions, in order to reduce unwanted chemical changes within the resist layer during the exposure [25].

2.2. NP cluster formation

Gold NCAs were fabricated by a chemical bonding driven self-assembly of gold NPs, purchased from Ted Pella, Inc., into the designed binding sites. The bare silicon surface of the lithographed substrate was functionalized to allow the chemical binding of the NP to the surface. The functionalization of the silicon surface was realized using two different protocols.

In the first protocol, the lithographed substrates surface were derivatized with 3% organosilane 3-amino-propyltriethoxy-silane (APTS) solution in ethanol for 90 min at room temperature. The modified plates were thoroughly rinsed with ethanol, baked at 110 °C for 10 min to stabilize further the silanized silicon silane, and then reacted with 1% glutaraldehyde (Glu) solution for 30 min at room temperature [25]. After thoroughly rinsing with milliQ water, the aldehyde-modified surfaces were conjugated with the Raman active heterobifunctional crosslinker 4-aminothiophenol (4-ATP) [4] in water solution (0.05 g/l 4-ATP) for 1 h and then rinsed. Free thiol moieties were thus available to covalently bind the NPs on the exposed silicon surfaces and the nanostructures was thus realized. Notice that the APTS—Glu linker was successfully adopted also to build up sensitive and stable Raman biosensing platforms in air and water environments [4].

In the second protocol, the thiols-driven stable connection between the bare gold NP surface and the silicon substrates was instead promoted directly by using a 3-mercapto-propyltriethoxy-silane (MPTS). The silicon substrates were incubated with 3% MPTS solution in ethanol for 90 min, and thus rinsed and backed, according to the first protocol.

In both cases, NP incubation was performed with consecutive steps of NP deposition (at 25 °C, for at least 3 h) and thorough rinsing in milli-Q water, to ensure a high NP density to be connected at the silicon surface, covalently. After each rinsing step the samples were dried under pure nitrogen gas. At the end of the treatment they were stored in the refrigerator (at 4 °C). If not specified otherwise, the chemicals were purchased from Sigma-Aldrich at analytical grade. Each step of the preparation was checked by AFM (see Section 3).

2.3. AFM measurements

Tapping-mode AFM images, using a cantilever with a spring constant, k, of 42 N/m, a scan rate of 0,3–0,7 Hz and an extremely sharp tip (nominal radius of curvature of 2 nm), were recorded by an Atomic Force Microscope Dimension Icon Bruker (c/o SNN-Lab—Sapienza Nanoscience & Nanotechnology Lab). All the AFM images shown herein are accompanied with a colour bar indicating the Z-range (height) of the features on the sample. Data analysys was performed by NanoSope Analysis Version 1.4 (Bruker Corporation).

2.4. Raman measurements

For the Raman spectroscopy investigation, the surface of the NCAs obtained by both the protocols were Raman-labelled with 4-ATP probe (Sigma-Aldrich) through a three hours incubation with a 0.05 g/l water solution of the molecule, followed by Milli Q water rinsing to remove the unbound molecules, and drying under pure nitrogen gas [5]. Raman measurements were performed with a LabRam HR Evolution Horiba Scientific, using a 100 × long working distance objective (N.A. = 0.80) for the confocal microscope. Surface Enhanced Raman Scattering (SERS) excitation was obtained with the 632.8 nm line of a He-Ne laser.The spectrometer was equipped with an automatic mapping stage with submicrometric precision. The spectroscopic images (SERS intensity maps) were obtained by collecting spectra at different, regularly disposed positions on the sample, whose control was allowed by the microscope coupled with the spectrometer. The step of the spectroscopic mapping was of 0.5 μm. The intensity of a selected Raman/SERS band was then calculated by integrating the spectrum around the band frequency and plotted against the spatial coordinates. The spectra were elaborated using LabSpec 6 and OriginPro 8 softwares and are herein presented without modifications. For the analysis of the intensity maps, a polynomial baseline (3rd degree) was subtracted to the spectra before their integration.

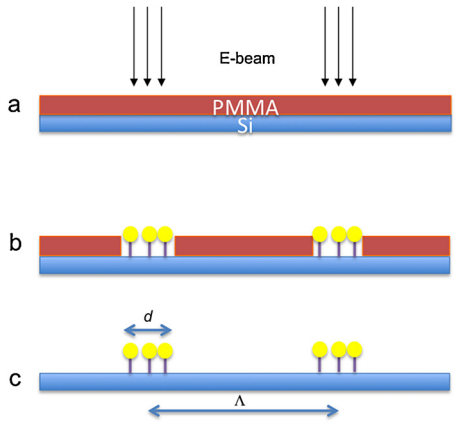

Fig. 1. Schematic process flow of the template-assisted assembly of NCAs. After the developing process, the e-beam patterning (a) is followed by the functionalization of the exposed binding sites to allow the chemical bonding guided self-assembly of NPs (b); the lift-off process (c) leaves on the substrate the particles patches of diameter d with a periodical spacing Λ.

3. Results and discussion

Several samples were prepared according to the protocol described in detail in Section 2, and schematized in Fig. 1. Briefly, EBL was applied on a thin layer of a positive resist laid on flat hydrophilic silicon surfaces (Fig. 1a). After the developing process, the exposed silanol surface was functionalized (Fig. 1b) to allow the NPs confinement onto the designed circular well areas at a fixed diameter d and periodical center-to-center spacing Λ (Fig. 1c).

In this section, we first report the AFM evaluation of the EBL patterning on several substrates; then we discuss the AFM topography together with the optical Raman features of representative microscale NCA assemblies.

3.1. Analysis of the ordered arrays

We considered four replicates of square arrays of wells (sectors) at varying d and Λ. Each lithographed sector (Fig. 2) was identified with a capital letter depending on the couple (Λ, d). We analyzed the sample surface by AFM after the lithographic process in order to compare the Computer Aided Design (CAD) nominal characteristics of the template patterns with the actual ones. Representative AFM images of the lithographic masks at two values of the area dose

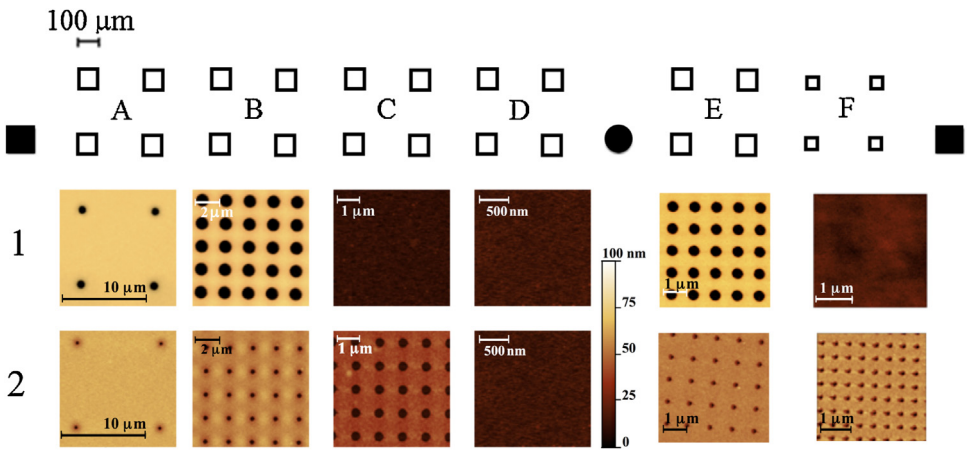

Fig. 2. The designed sectors arrangement tamplate (four replicates for sector) togheter with the represenative AFM topography of A–F sectors, lithographed using an area dose value of 100 μC/cm^2 (row 1) and of 20 μC/cm^2 (row 2).

Table 1
Geometric features of the sectors realized at variable e-beam dose. Standard deviations on the experimental *d* values are calculated on 5 profiles for each sector. The parameter Λ-*d* is critical for a successful design of the lithographic mask (see Section 3.1).

Sector	Dose value (μC/cm^2)	Λ (μm)	Nominal *d* (μm)	Λ-*d* (μm)	measured *d* (μm)
(A,1)	100	10	0.500	9.500	0.70 ± 0.06
(A,2)	20	10	0.250	9.750	0.25 ± 0.02
(A,2)[a]	20	10	0.50	9.500	0.44 ± 0.03
(B,1)	100	2	0.500	1.500	0.87 ± 0.07
(B,2)	20	2	0.250	1.750	0.30 ± 0.03
(B,2)[a]	20	2	0.50	1.500	0.57 ± 0.04
(C,1)	100	1	0.500	0.500[b]	Bowl
(C,1)[a]	100	1	0.250	0.750	0.7 ± 0.1
(C,2)	20	1	0.250	0.750	0.33 ± 0.05
(D,1)	100	0.75	0.500	0.250	Bowl
(D,2)	20	0.75	0.500	0.250[c]	Bowl
(D,2)[a]	20	0.75	0.250	0.500	0.23 ± 0.07
(E,1)	100	1	0.250	0.750	Not reproducible
(E,2)	20	1	0.125	0.850	0.040 (not uniform)
(F,1)	100	0.50	0.250	0.250	Bowl
(F,2)	20	0.50	0.125	0.375	0.040 (not uniform)

[a] Sectors with nominal *d* halved or doubled with respect to those shown in Fig. 2.
[b] RS_{100}.
[c] RS_{20}.

(100 μC/cm^2 and 20 μC/cm^2) are shown in Fig. 2, the experimental average *d* values are compared with the nominal ones in Table 1.

We did not find significant discrepancies between the nominal and measured Λ. Conversely, nominal and experimental *d* values differed significantly for both doses (Table 1), and such differences increased at smaller Λ. Moreover, at the higher doses, the correspondence between the actual and the nominal masks was significantly deteriorated (see for example, the *d* values of the sectors with the higher Λ, A and B in Table 1). In this respect, Fig. 3 shows the AFM images and the corresponding height profiles representatives of sectors A an B demonstrating the effect of the e-beam process on the thickness of the resist coating on silicon substrates. As shown in the AFM profiles of Fig. 3b and c, the e-beam writing at the intense dose of 100 μC/cm^2 resulted in symmetric wells, regularly disposed on the thin resist film, although their effective *d* values resulted significantly larger than the nominal ones. In these cases, the binding site of the NP is only the silicon surface exposed at the bottom of the well.

This effect of enlargement of the single site (named intraproximity) is due to the strong electron scattering [23]. With decreasing Λ the scattering begins to affect the shape of the sites (interproximity effect) [23]. These effects cause an uneven degradation of the resist within individual sites as well as of the thickness of the resist lithographed (compare the resist thicknesses of Fig. 3a–c).

At fixed Λ (sectors A and B) a decrease of the nominal *d* by a factor of two, results in a dramatic reduction of the difference between nominal and measured *d*. Since a shorter exposure time is needed to write a smaller well, for the sectors designed at smaller *d* the electron scattering was consequently reduced, and the mismatch between theoretical and measured parameters diminished. This could have been expected, since the energy absorbed by the resist depends on both exposure time and e-beam intensity, whose product defines the dose. The same considerations hold for the AFM analysis of the sectors C and D, which are realized at Λ halved compared to A and B, respectively. At the higher dose, the interproximity effect completely degraded the resist of the sector, so that only one single tank is formed (see Fig. 2). The same happens for the sector (F,1) in which both Λ and *d* were halved by a factor of two compared to (C,1) (Table 1).

In practice, because of the proximity effect, an empirical dose-dependent threshold value could be defined for the resist sinking, RS_{dose} = Λ-*d*, below which we cannot solve individual NP binding areas using EBL. At doses of 100 μC/cm^2 RS_{100} is ~0.5 μm. At the dose value of 20 μC/cm^2, RS_{20} is expected to be smaller, and in fact we can get more densely structured arrays, (masks C and F, Fig. 2). The RS_{20} value is ~0.25 μm.

However, to obtain smaller *d* the dose cannot be further reduced without risking that the area to be excavated is not broken down

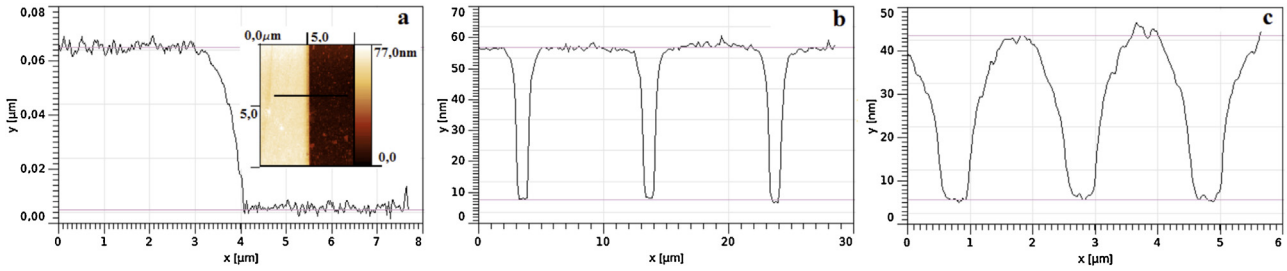

Fig. 3. AFM profiles to evaluate the thickness of the resist film after the spin-coating process (a), and after the e-beam process at dose of 100 μC/cm^2 on the sectors (A,1) and (B,1), corresponding to Λ = 10 μm (b) and Λ = 2 μm (c). See also Table 1.

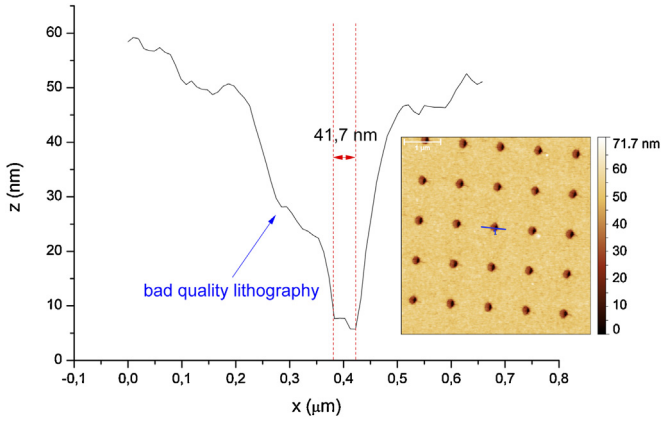

Fig. 4. AFM analysis of a part of the lithographed E sector (Λ = 1 μm; *d* = 0.125) realized at e-beam dose 20 μC/cm^2. The region between the red dashed lines indicates the resist area completely developed that can be functionalized effectively, much smaller than expected. (For interpretation of the references to colour in this figure legend, the reader is referred to the web version of this article.).

completely. This is what happened in sector E: at dose 20 μC/cm^2, the AFM profilometry in Fig. 4, shows a large asymmetric degradation of the resist, partially overlapping the area designed for NP functionalization. In these cases, it may be necessary to increase the dose by increasing the exposure time (i.e. dwell time). In fact, by increasing the intensity of the e-beam the measured average diameter is much larger, irregular (sector (E,1) in Fig. 2) and poorly reproducible.

This study shows that by properly adjusting the dose values very accurate and reproducible micro-structured substrates can be prepared. Based on these results, we prepared the masks (A,1) (B,1) and (B,2)* and used them as templates to successfully arrange long-range ordered micrometric and submicrometric NP clusters, 2 and 10 micrometer spaced.

3.2. Analysis of the gold NCAs

The lithographic patterns were functionalized using two protocols based on either APTS/Glu/4-ATP or MPTS linkers (see Section 2.2). After the NP deposition, and having lifted off the resist, we obtained a regular 2D layout of NP clusters since the NPs are arranged only in the well binding sites (Fig. 1). The AFM topography of the NCA of sectors A and B is shown in Fig. 5. In Fig. 5a the long range order is acceptable, but apparently the number of NPs linked with the APTS—Glu—4-ATP is rather low. Conversely, Fig. 5b shows that using MPTS linkers a regular array of densely packed NP clusters is obtained. The AFM profiles on a representative single micrometric NP clusters of (B,1) after the binding site being functionalized with 60 nm gold NPs through MPTS linker is reported in Fig. 6a. In the same array the possible formation of an over layered excess of NPs is also shown in Fig. 6b. We cannot rule out that the NP sometimes found stacked, forming multilayered clusters, did not come from the rare presence of small aggregates of NP already present in the incubation solution, rather than being formed by physisorption during the incubation process. Notably, we can instead exclude the presence of impurities at atomic resolution as determined by AFM topography and the phase image (Fig. 5b). A challenge still open it is to fine control the vertical organization of these NPs clusters.

The comparatively different NP binding yield we observe in Fig. 5a and b reflects the effect of differing the number of steps and chemical involved in the two protocols of NCA fabrication protocols, and, in turn a different anchoring agent concentration. Notably, the samples prepared by covalently binding NPs via MPTS links are very stable, also in water for several days.

Among the advantages which influence the outcome of the functionalization, there could be the low number of steps and chemicals involved in the protocols and the stability of the product: therefore the protocol where it is involved the MPTS is favorable in this respect. Both the protocols have the vantage of exposing a gold particle surface available to physi- or chemi-sorb different analytes although the tight arrangement in two-dimensional clusters of the NP reduces the binding area portions available for capturing the analytes. Alternatively, the overall gold NP surface could be engineered to bind the analytes (e.g. proteins and cells) in solutions [26] and then captured by the arrays (e.g. APTS-Glu linkers) for the microanalysis.

The potential of these NCA as sensitive Raman spectroscopy platforms was probed by following the Raman signal of 4-ATP molecules localized onto the NPs surface. Herein we focused on the sector (A,1), whose Λ resulted large enough to prevent any possible optical interferences and to optimize the realization of spectroscopic mapping. The main results are shown in Fig. 7.

A representative Raman spectrum of a NP cluster of the array displaying Λ = 10 μm and d = 1 μm features, probed through the Raman porter 4-ATP is compared in Fig. 7a with the traditional Raman spectrum of the same molecule (see Ref. [5] for the band assignment). As expected, the Raman cross-section of 4-ATP when covalently linked to the NP clusters surface results strongly increased due to the SERS phenomenon [1,4]. The reason of the molecular spectroscopic signal enhancement is the surface plasmon resonance of these gold nanostructures: the oscillation of the surface electron gas in the metal nanostructure gives rise to a strong increase of the local electromagnetic field at the metal-dielectric interface. For this reason, the spectral response of the molecules bound to the Np surface appears as if they were illuminated by a much stronger field [1].

A reasonable way to evaluate the efficiency of a plasmonic substrate in signal enhancing is to calculate the enhancement factor (EF), namely the ratio of SERS and Raman spectroscopic intensity per single molecule. In our case, the spectroscopic intensity is obtained by integrating either the whole SERS spectrum (*overall* EF) or the strong C-S stretching band of 4-ATP, centered at

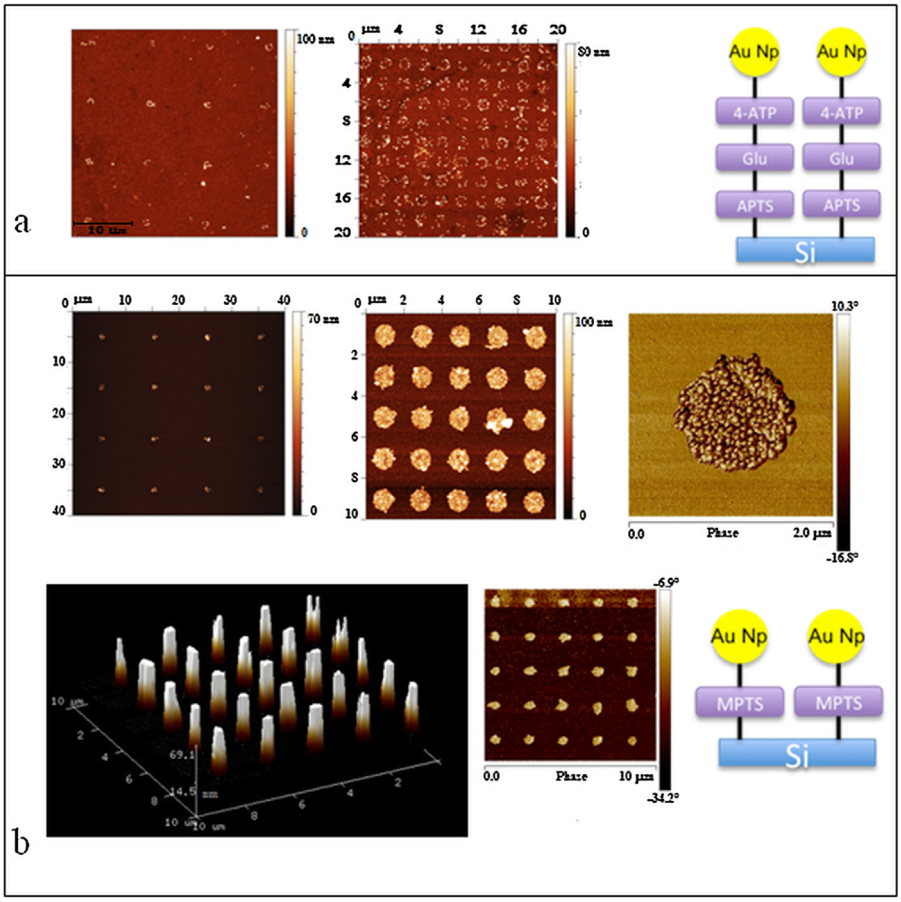

Fig. 5. AFM images of NCA obtained from A and B sectors using APTS + Glu + 4-ATP (panel a) or MPTS (panel b) for linking the NPs onto the Si-OH binding sites.
Panel a, from left to right: the topography of array areas from (A,1) and (B,1) sectors specified in Table 1, and the functionalization scheme.
Panel b, on the up side, from left to right: the topography of array portions of (A,1) and (B,1), and the Phase image of a representative NP cluster from (B,1); on the bottom side, from left to right: the three-dimensional topography of an array portion from (B,2)* specified in Table 1, the corresponding Phase image, and the functionalization scheme.

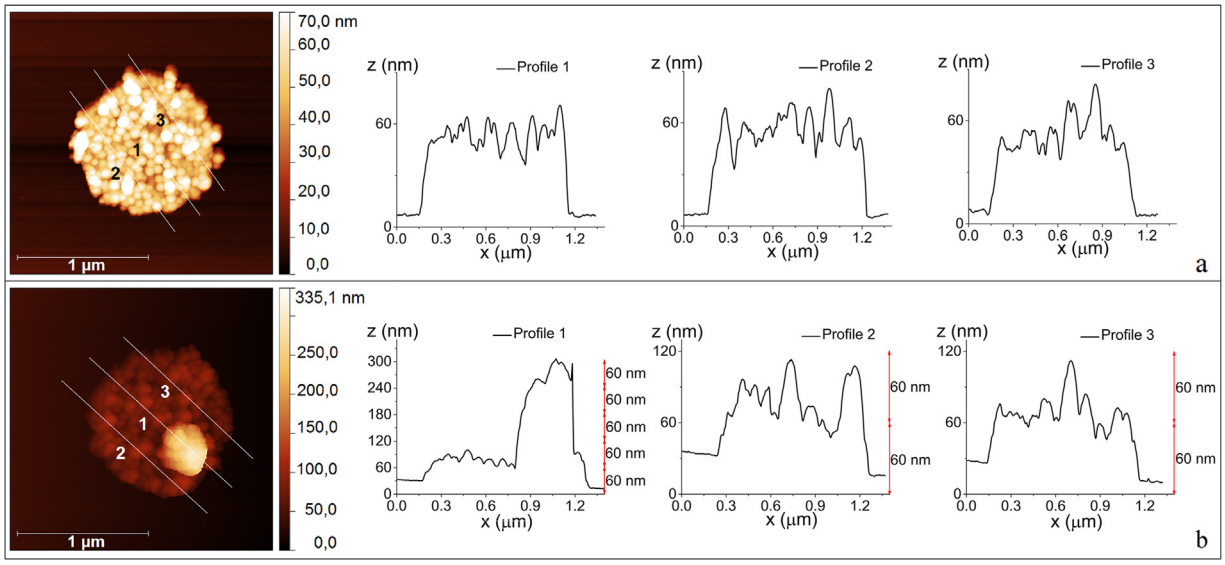

Fig. 6. Nanoparticles cluster from sector (B,1), Λ=2 µm and d = 1 µm, with three height profiles. The z-values are in accordance with the overlap of several nanoparticles sized 60 nm, well compact with each other to form discs to one (a) or sometimes even more layers of nanoparticles (b).

1088 cm^{-1} in the Raman spectrum and red-shifted to 1079 cm^{-1} in the SERS spectrum (*band* EF). The number of molecules contributing to the spectroscopic signal is in both cases estimated via geometrical considerations (see Ref. [13] for details). SERS signal amplification is known to benefit of two contributions: one electromagnetic, arising from the substrate plasmonic resonance that enhances the local field around the molecules, and one chemical, coming from the metallic substrate-molecule charge transfer.

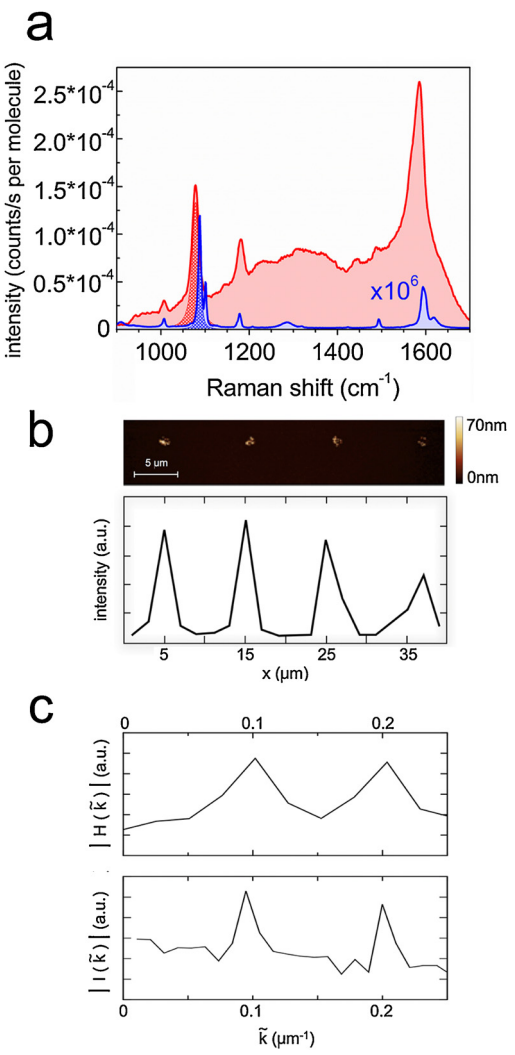

Fig. 7. Panel a: the SERS spectrum (red) of 4-ATP linked to the NP clusters, assembled on the lithographed binding sites, is compared to the Raman spectrum (blue) of the 4-ATP Raman spectrum. Both spectra are normalized to the number of molecules contributing to the spectroscopic signal (i.e. present in the scattering volume). The Raman spectrum is multiplied by a scaling factor of 10^6. The integrated intensities used to estimate the enhancement factors are evidenced: the whole spectral integral is coloured in light red (SERS) and light blue (Raman spectrum), while the area of the band centered at 1079 cm^{-1} (1088 cm^{-1} in Raman spectrum), estimated through a Lorentzian fitting, is evidenced with the squared pattern in red and blue respectively. Panel b: a representative SERS intensity trend measured along a row of the sector A ($\Lambda = 10\,\mu m$, $d = 1\,\mu m$), compared with the corresponding AFM topography. Panel c: fast Fourier transform (FFT) obtained on AFM signal of sector A (upper plot, |H(k)|) is compared to the FFT of the SERS signal on the same sector (lower plot, |I(k)|). The peak of the periodicity of 10 mm (centered at 0.1 μm^{-1}) and the second armonic (at 0.2 μm^{-1}) are visible. The comparatively larger width of the AFM FFT peaks is related to the different size of the frame measured (40 mm and 75 mm for AFM and SERS acquisition, respectively). (For interpretation of the references to colour in this figure legend, the reader is referred to the web version of this article.)

When considering the overall enhancement factor, we are taking into account both the mechanisms. This EF estimate is more appropriate for molecules covalently bound to the metal surface. On the other hand, the band EF is expected slightly smaller, as we chose for the integration the C—S stretching band, which is known to be enhanced only by electromagnetic mechanism: this can be considered representative for molecule physisorbed to the metal surface. For this kind of substrates, as reported in Fig. 7a, we found an overall EF of $\sim 1\times10^7$, which is quite notable when compared to the EF values reported in literature for gold based substrates [15]. The strong intensity of the SERS C—S stretching band allowed us to spatially resolve the presence of the clusters, and thus to find the full correspondence existing between the AFM topography and SERS intensity maps. Fig. 7b shows indeed that the SERS intensity is displayed along the NP cluster rows according to the periodicity of the array. Some significant drop or raise in SERS intensity (>20%) was detected and is related to the occurrence of isolated NPs assembly exhibiting uneven surface packing, as confirmed both by optical inspection and AFM analysis (Fig. 6b). The large number of clusters per $100\times100\,\mu m^2$ area (100 clusters for the A sectors) enables to discard the worst data, thus ensuring a contained variability of the SERS intensity, within roughly 20% on ensembles up to 30 clusters, measured consequently. At the best of our knowledge, it is not common to estimate the reproducibility of the Raman signal reproducibility on plasmonic assemblies, and we believe that the result of an *overall* EF of $(1.1\pm0.2)\times10^7$, and of a band EF of $(0.30\pm0.06)\times10^7$, is to be considered very positively [6,15]. The latter result confirmed the previously mentioned idea that NPs clusters of micrometric and controlled areas can provide quite regular, reproducible, and highly enhanced Raman signals.

Ultrasensitive detection technologies require the ability to integrate fast sensing, low sample and reagent volumes, reduction of the size of equipment, possibility of portable devices and parallel operation for multiple and automated analyses [26,27]. Within this challenge, the results presented herein, on the possibility of realizing micrometric patches of closely packed NP over micrometric periodical inter-patch distance, represents a further step toward the construction of efficient Lab-on-a-chip integrated systems [27].

4. Conclusions

In this work we discussed the realization of accurate and reproducible e-beam lithographic patterns, that have been exploited in order to isolate regularly-disposed areas on a Si substrate. We tested different protocols of surface functionalization, used to induce the covalent self-assembled aggregation of gold NPs. The characterization of the patterns was realized by AFM measurements, which showed the presence of dense, highly packed NP clusters of micrometric size and spacing regularity. High and reproducible optical signals displayed on the corresponding array periodicities were enlightened by microRaman analysis. The demonstrated approach may be useful particularly in the aim of realizing benchmark NCAs, featured as stable and reproducible gold NP clusters in the mesoscopic scale, leading to the challenging production of improved opto- and conductive-microfluidic multiplex-sensing.

References

[1] J.N. Anker, W.P. Hall, O. Lyandres, N.C. Shah, J. Zhao, R.P. Van Duyne, Biosensing with plasmonic nanosensors, Nat. Mater. 7 (2008) 442–453.
[2] M.P. Cecchini, V.A. Turek, J. Paget, A.A. Kornyshev, J.B. Edel, Self-assembled nanoparticle arrays for multiphase trace analyte detection, Nat. Mater. 12 (2013) 165–171.
[3] B. Yan, S.V. Boriskina, B.M. Reinhard, Design and implementation of noble metal nanoparticle cluster arrays for plasmon enhanced biosensing, J. Phys. Chem. C 115 (2011) 24437–24453.
[4] F. Domenici, A.R. Bizzarri, S. Cannistraro, Surface-enhanced Raman scattering detection of wild-type and mutant p53 proteins at very low concentration in human serum, Anal. Biochem. 421 (2012) 9–15.
[5] F. Domenici, A.R. Bizzarri, S. Cannistraro, SERS-based nanobiosensing for ultrasensitive detection of the p53 tumor suppressor, Int. J. Nanomed. 6 (2011) 2033–2042.
[6] B. Yan, S.V. Boriskina, B.M. Reinhard, Optimizing gold nanoparticle cluster configurations ($n \leq 7$) for array applications, J. Phys. Chem. C Nanomater. Interfaces 115 (2011) 4578–4583.
[7] K. Saha, S.S. Agasti, C. Kim, X. Li, V.M. Rotello, Gold nanoparticles in chemical and biological sensing, Chem. Rev. 112 (2012) 2739–2779.
[8] E. Boisselier, D. Astruc, Gold nanoparticles in nanomedicine: preparations, imaging, diagnostics, therapies and toxicity, Chem. Soc. Rev. 38 (2009) 1759–1782.

[9] Y.-C. Yeh, B. Crerana, V.M. Rotello, Gold nanoparticles: preparation, properties, and applications in bionanotechnology, Nanoscale 4 (2012) 1871–1880.
[10] P.K. Jain, X. Huang, I.H. El-Sayed, M.A. El-Sayed, Noble metals on the nanoscale: optical and photothermal properties and some applications in imaging, sensing, biology, and medicine, Acc. Chem. Res. 41 (2008) 1578–1586.
[11] E.S. Kooij, W. Ahmed, C. Hellenthal, H.J.W. Zandvliet, B. Poelsem, From nanorods to nanostars: tuning the optical properties of gold nanoparticles, Colloids Surf. A 413 (2012) 231–238.
[12] S. Mühlig, D. Cialla, A. Cunningham, A. März, K. Weber, T. Bürgi, F. Lederer, C. Rockstuhl, Stacked and tunable large-scale plasmonic nanoparticle arrays for surface-enhanced raman Spectroscopy, J. Phys. Chem. C 118 (2014) 10230–10237.
[13] C. Fasolato, F. Domenici, S. Sennato, F. Mura, L. De Angelis, F. Luongo, F. Costantini, F. Bordi, P. Postorino, Dimensional scale effects on surface enhanced Raman scattering efficiency of self-assembled silver nanoparticle clusters, Appl. Phys. Lett. 105 (2014) 073105-1–073105-4.
[14] C. Fasolato, F. Domenici, F. Brasili, F. Mura, S. Sennato, L. De Angelis, E. Mazzi, F. Bordi, P. Postorino, Self-assembled nanoparticle aggregates: organizing disorder for high performance surface-enhanced spectroscopy, AIP Conf. Proc. 1667 (2015) 020012-1–020012-7.
[15] B. Yan, A. Thubagere, W.R. Premasiri, L.D. Ziegler, L. Dal Negro, B.M. Reinhard, Engineered SERS substrates with multiscale signal enhancement: nanoparticle cluster arrays, ACS Nano 3 (2009) 1190–1202.
[16] M. Alba, N. Pazos-Perez, B. Vaz, P. Formentin, M. Tebbe, M.A. Correa-Duarte, P. Granero, J. Ferr-Borrull, R. Alvarez, J. Pallares, A. Fery, A.R. de Lera, L.F. Marsal, R.A. Alvarez-Puebla, Macroscale plasmonic substrates for highly sensitive surface-enhanced raman scattering, Angew. Chem. Int. Ed. 52 (2013) 6459–6463.
[17] I. Utke, S. Moshkalev, P. Russell (Eds.), Nanofabrication Using Focused Ion and Electron Beams, Principles and Applications, Oxford University Press, Oxford, 2012.
[18] G.R. Brewer (Ed.), Electron-Beam Technology in Microelectronic Fabrication, Academic Press Inc., London, 1980.
[19] U.S. Tandon, W.S. Khokle, Patterning of Material Layers in Submicron Region, John Wiley & Sons, New York, 1994.
[20] C.R.K. Marrian, D.M. Tennant, Nanofabrication, J. Vac. Sci. Technol. A 21 (2003) S207–S215.
[21] B.G. Prevo, D.M. Kuncicky, O.D. Velev, Engineered deposition of coatings from nano-and micro-particles: a brief review of convective assembly at high volume fraction, Colloids Surf. A 311 (2007) 2–10.
[22] S.H. Kim, S.Y. Lee, S.M. Yang, G.R. Yi, Self-assembled colloidal structures for photonics, NPG Asia Mater. 3 (2015) 25–33.
[23] S.-F. Hu, K.-D. Huang, Y.-M. Wan, C.-L. Sung, Proximity effect of electron beam lithography on single-electron transistors, Pramana J. Phys. 67 (2006) 57–65.
[24] M.A. Mohammad, M. Muhammad, S.K. Dew, M. Stepanova, Fundamentals of electron beam exposure and development, in: M. Stepanova, S. Dew (Eds.), Nanofabrication, Springer-Verlag, Wien, 2012.
[25] C.M. Halliwell, A.E.G. Cass, A factorial analysis of silanization conditions for the immobilization of oligonucleotides on glass surfaces, Anal. Chem. 73 (2001) 2476–2483.
[26] C.P. Jia, X.Q. Zhong, B. Hua, M.Y. Liu, F.X. Jing, X.H. Lou, S.H. Yao, J.Q. Xiang, Q.H. Jin, J.L. Zhao, Nano-ELISA for highly sensitive protein detection, Biosens. Bioelectron. 24 (2009) 2836–2841.
[27] F. Costantini, A. Nascetti, R. Scipinotti, F. Domenici, S. Sennato, L. Gazza, F. Bordi, N. Pogna, C. Manetti, D. Caputo, G. de Cesare, On-chip detection of multiple serum antibodies against epitopes of celiac disease by an array of amorphous silicon sensors, RSC Adv. 4 (2014) 2073–2080.